

A real-time, scalable, fast and highly resource efficient decoder for a quantum computer

Ben Barber,¹ Kenton M. Barnes,¹ Tomasz Bialas,¹ Okan Buğdaycı,¹ Earl T. Campbell,^{1,2} Neil I. Gillespie,¹ Kauser Johar,¹ Ram Rajan,¹ Adam W. Richardson,¹ Luka Skoric,¹ Canberk Topal,¹ Mark L. Turner,¹ and Abbas B. Ziad¹

¹*Riverlane, Cambridge, UK.*

²*Department of Physics and Astronomy, University of Sheffield, UK*

(Dated: September 2023)

Quantum computers promise to solve computing problems that are currently intractable using traditional approaches. This can only be achieved if the noise inevitably present in quantum computers can be efficiently managed at scale. A key component in this process is a classical decoder, which diagnoses the errors occurring in the system. If the decoder does not operate fast enough, an exponential slowdown in the logical clock rate of the quantum computer occurs. Additionally, the decoder must be resource efficient to enable scaling to larger systems and potentially operate in cryogenic environments. Here we introduce the Collision Clustering decoder, which overcomes both challenges. We implement our decoder on both an FPGA and ASIC, the latter ultimately being necessary for any cost-effective scalable solution. We simulate a logical memory experiment on large instances of the leading quantum error correction scheme, the surface code, assuming a circuit-level noise model. The FPGA decoding frequency is above a megahertz, a stringent requirement on decoders needed for e.g. superconducting quantum computers. To decode an 881 qubit surface code it uses only 4.5% of the available logical computation elements. The ASIC decoding frequency is also above a megahertz on a 1057 qubit surface code, and occupies 0.06 mm² area and consumes 8 mW of power. Our decoder is optimised to be both highly performant and resource efficient, while its implementation on hardware constitutes a viable path to practically realising fault-tolerant quantum computers.

I. INTRODUCTION

Quantum computers have the potential to solve computational problems that are out of reach of classical computers. However, to realise this potential all architectures need to deal with the fragility of their quantum bits (qubits) [1–4]. Qubits are highly likely to interact with the environment, or decohere, which leads to a loss of information stored and errors in the corresponding computation. Fortunately, Quantum Error Correction (QEC) protocols enable fault-tolerant computation in the presence of this noise. By adding redundancy, information can be protected by encoding it into logical qubits. Errors can still corrupt the information in this setting, and so a signal is periodically generated from the logical data, which characterises the errors that have occurred. This signal, called a syndrome, is processed by a decoder running on classical hardware whose output is the best guess of the error that has occurred on the logical data. This information is passed back to the control system so that corrective steps can be taken in subsequent operations.

QEC must be performed continuously creating a stream of syndrome data, and therefore, as systems scale and lower logical error rates are required, the amount of data that needs to be processed by a decoder increases significantly. For large computations, this will require real-time decoders that can process the data at the rate it is received to avoid the creation of a backlog that grows exponentially with the depth of the computation [5, 6], ultimately slowing it down to a halt. Superconducting quantum devices, for example, generate a round of syndrome data in less than 1μs (a rate of MHz), setting a

stringent requirement on decoder speed. Future utility-scale quantum computers will therefore require an optimised hardware decoder integrated in a tight loop at the heart of the control system.

There are several fast and accurate decoders implemented in software languages such as Python and C++ [7–9]. Most experiments to date have used software decoders to decode offline [2, 10–12]: rather than decoding in real-time, the syndrome data is processed after the experiment has concluded. However, real-time decoding is essential for logic branching required to implement non-Clifford gates to realise the full potential of quantum computation [13]. Even if software decoders were run during experiments, the non-deterministic latency of software would make it difficult to tightly integrate with the control system of a quantum computer. Hardware decoders based on Field Programmable Gate Arrays (FPGAs) or Application Specific Integrated Circuits (ASICs) can execute within a deterministic number of clock cycles, and also tightly integrate into control systems. Therefore, to meet the challenge of developing real-time decoders, the community has begun to implement decoders on dedicated hardware, specifically FPGAs [14–17], and provide models of ASIC implementations [16, 18].

FPGAs will be sufficient for decoding problems in the medium term. They provide the flexibility to adapt and change implementations of decoders, and can be easily integrated into control systems. This level of flexibility will clarify the parameters that need to be optimised to improve the overall performance of the system. Until recently, only small instances of surface code decoders have been implemented on FPGAs [14, 16, 17]. Promising re-

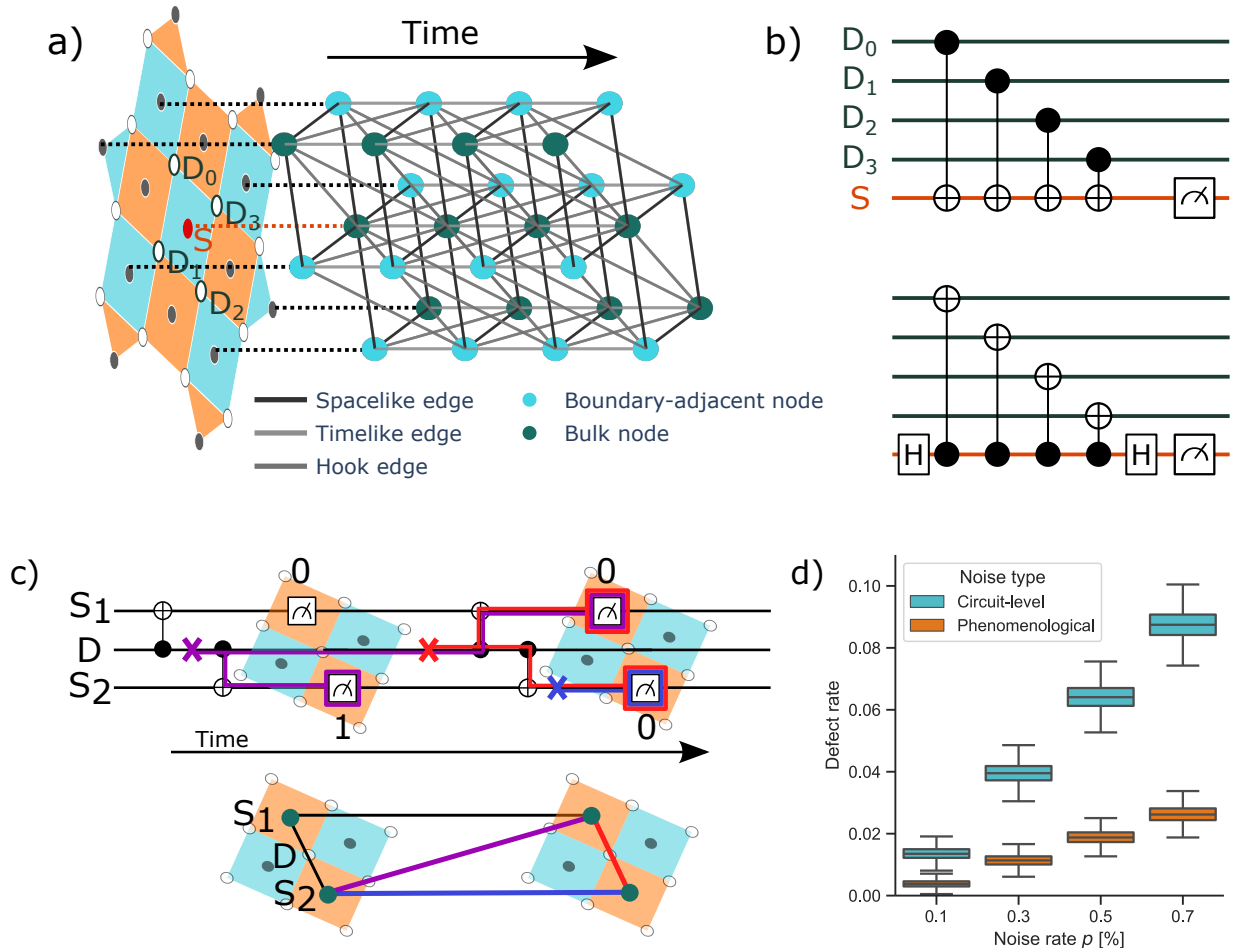


FIG. 1. Quantum Error Correction using a rotated planar surface code. (a) The logical information is encoded by combining multiple physical qubits laid out on a surface (orange and teal grid). The physical qubits can be divided into data qubits (D_i , empty circles) encoding the state, and syndrome qubits (S , full circles). Repeated measurements of syndrome qubits provides information about errors. Possible error mechanisms can be represented by a graph in which nodes represent differences between syndrome measurements in consecutive rounds (potential defects) and edges represent error mechanisms that create the corresponding pair of defects (see Section II C for more details). Error mechanisms that trigger only one defect (teal nodes) are in addition connected to a fictitious boundary node (not drawn). Z and X parity check patches (teal and orange squares) protect against X and Z errors respectively and result in two equivalent and disjoint graphs – only the Z check graph is shown here. (b) Quantum circuits to measure the Z (top) and X (bottom) parity checks. The circuit is continuously repeated until the computation ends and all qubits are measured out. (c) Two rounds of syndrome measurements displaying only a part of the circuit that involves a single data and two syndrome qubits (top). The possible error mechanisms are depicted with different colours: data (red), measurement (blue), and hook (purple) errors and result in corresponding edges in the decoding graph (bottom). (d) Comparison of defect rate for phenomenological and circuit-level noise models with the same noise rate on distance 23 rotated planar surface code. While the decoding of circuit-level noise is made more complicated by the presence of hook edges, it also results in approximately 3.5 times more defects due to more possible error locations.

sults have appeared on larger examples, where decoding one round of syndrome data of a 881 qubit surface code in under $1 \mu\text{s}$ was demonstrated [15]. However, only a toy noise model was used and the design required significant FPGA resources.

FPGA systems have high per unit cost and power consumption and so are not long-term solutions for scaling to millions of qubits. Once the architecture design of a fault-tolerant quantum computer is understood, cost-effective scaling can only be achieved with ASICs, which additionally provide improved performance and power

consumption at the cost of longer development times. ASICs will also be needed if tight integration is required between decoders and control systems in a cryogenic environment [19].

One of the central challenges facing the community is how to efficiently scale Quantum Processing Units (QPUs) to larger numbers of qubits, particularly the numbers required for fault-tolerant quantum computing. To meet this challenge, it is crucial to make as many components of the QPU as efficient and simple as possible, including the decoder. We introduce the Collision

Clustering (CC) decoder to satisfy these and the above requirements. It is a clustering decoding algorithm designed to have low FPGA utilisation and low ASIC power and area, while at the same time performant enough to keep up with the syndrome generation time of the QPU. To demonstrate this, we implement the CC decoder on a Xilinx Ultrascale+ XCVU3P FPGA and a modern 12 nm FinFET ASIC process node [20]. Assuming a circuit-level noise model with error rate $p = 0.1\%$, on the FPGA we decode a 881 qubit surface code in 810 ns using only 4.5% of the available computational elements (Logic LUTs) and 10 KB of memory. Moreover, we obtain a threshold of 0.78%. Our implementation on the ASIC decodes 1057 qubit surface code in 240 ns, using only 0.06 mm² of area and 8 mW of power.

II. BACKGROUND

A. Surface codes

Surface codes are a family of codes that have been studied extensively since their discovery over twenty years ago [21]. They can be implemented on 2D architectures with fixed nearest neighbour interactions, e.g. superconducting qubits, and there are known techniques to perform fault-tolerant computation [13, 22–24]. Surface codes also have high thresholds that have proved difficult to improve upon [25], meaning they have been implemented in several near term error correction experiments [2, 10, 11]. Combined, these observations make surface codes likely candidates for the error correction schemes used in the first fault-tolerant devices. In this work, we focus mainly on the rotated planar surface code (Fig. 1) [26].

The surface code is defined on a square lattice by operators that check the parity of sets of qubits in either the Pauli Z or X basis (see Fig. 1). These operators are measured repeatedly to generate the syndrome and project the qubits into a logical computation space. We call a single round of measuring all the parity check operators a round of syndrome measurements, and the measurement data generated a round of syndrome data. For the rotated planar code, a round of syndrome measurements requires $d^2 - 1$ syndrome qubits for a $d \times d$ surface code, giving a total of $2d^2 - 1$ qubits. The logical qubit is defined by logical Pauli operators forming a path between opposite boundaries. The *distance* of the surface code is the minimum number of Pauli operators in such a logical operator, which is just the side length d of the lattice.

Quantum algorithms demonstrating industrially relevant advantage over classical computation consistently require at least a trillion reliable quantum operations [27–32]. Therefore, any error correction scheme needs to be able to generate logical error rates of 10^{-12} or better. To achieve these error rates, we can use larger distance surface codes which exponentially suppress errors. In addition to using more physical qubits, this significantly in-

creases the amount of information that needs to be processed by the decoder. The time to generate a round of syndrome data remains constant, so to avoid the backlog problem we need to solve a harder problem in the same amount of time. It is therefore important to demonstrate decoding performance on large distance surface codes.

B. Decoding the surface code

The core challenge in quantum error correction is to preserve a logical state, known as logical memory [2]. For the surface code, this involves initialising a logical state, performing several rounds of syndrome measurements, and finishing with a logical Pauli measurement. We are concerned with the overall effect of errors on the outcome of the logical measurement. Therefore, the decoding problem is to determine whether the logical measurement has been flipped given the observed syndrome and logical measurements.

The circuit used to measure the parity check operators (see Fig. 1b) has a syndrome qubit that is reset and measured, single qubit gates, and two-qubit gates that map errors onto the syndrome qubit. In addition to the noise on the data qubits, each of these operations potentially introduces additional noise mechanisms. This is why the parity check operators are measured repeatedly, forming the syndrome. If no errors occur, these measurements produce the same results in consecutive rounds. Therefore, an error is detected when there is a change in the outcome of a measurement from one round to the next. We call these changes in measurement outcomes *defects*.

The syndrome is best represented in a decoding graph (Fig. 1a). The vertices of the decoding graph correspond to all possible defects. If an error mechanism triggers two defects, we connect the corresponding vertices by an edge. Some error mechanisms only trigger a single defect e.g. errors on the data qubits on the boundaries of the lattice. To capture these error mechanisms, we connect the corresponding defects to virtual boundary vertices. By taking the XOR of consecutive rounds of syndrome measurements, we can identify the syndrome with the set of defects that have been triggered. The decoding problem can now be rephrased as determining the most likely logical measurement given the defects in the decoding graph.

C. Noise model

Noise models vary both in the level of errors they produce as well as the types of error mechanism that can occur, which have a significant impact on the decoder performance. Throughout this work, we sample syndromes using the Clifford circuit simulator Stim [33] with several independent noise channels, parameterized by a single probability p , that give a rough approximation of noise

channels characteristic of a generic superconducting device:

- Depolarisation of both qubits after each 2-qubit gate with probability p .
- Depolarisation of each idle qubit and after each single-qubit gate, including measurement and reset operations, with probability $p/10$.
- Randomly change the result of a measurement with probability p .

We use the parametrisation where depolarising a single qubit means applying a random non-identity Pauli error:

$$\mathcal{E}(\rho) = (1 - p)\rho + \frac{p}{3}(X\rho X + Y\rho Y + Z\rho Z) \quad (1)$$

Depolarising two qubits means applying one of the 15 non-identity two qubit Pauli errors uniformly at random (so that each two qubit error occurs with probability $p/15$).

Our circuit-level noise model generates a larger quantity and variety of defects than the phenomenological noise model [34] which abstracts away the details of generating the syndrome. On a distance $d = 23$ rotated planar surface code with $p = 0.1\%$, our noise model produces defects at a rate of 1.35% (or about 3.6 defects per round), while the phenomenological noise model [15] with the same probability p produces defects at a rate of 0.38% (or about 1 defect per round, see Fig. 1d).

III. THE COLLISION CLUSTERING DECODER

We introduce the Collision Clustering (CC) decoding algorithm to meet the various challenges set out in Section I. CC is an example of a clustering decoding algorithm. Given a decoding graph with a set of defects, CC takes the set of defects and partitions it into distinct subsets, known as clusters, which can be explained locally. Each cluster is then analysed to determine its effect on the logical measurement. To do this, CC uses a reference logical operator, which we take to be a logical Pauli operator running along one of the boundaries of the lattice. We call the corresponding boundary in the decoding graph the logical boundary. After clustering, the correction bit returned by CC is the parity of the number of odd sized clusters that touch the logical boundary.

Before we describe how CC generates its clusters, we turn to another clustering decoding algorithm, Union-Find, first proposed by Delfosse et al. [35]. In the Union-Find micro-architecture of Das et al. [18], a key component is the data structure used to help keep track of the state of emerging clusters, called the *spanning tree memory* (STM). Based on our simulations of their design, we identified that the main performance bottleneck was reading from and writing into the STM data structure. This suggests using a different data structure to help keep

track of the state of emerging clusters that does not require a lot of memory could be beneficial in a clustering decoding algorithm.

A. Cluster Growth Stack and Parent Table

In the CC decoder, each defect begins in its own cluster. The clusters then *grow* in the decoding graph, and, if two clusters overlap, they *merge* to form one cluster. A cluster continues to grow so long as it has an odd number of defects within it, or until it touches one of the open boundaries of the code. Once all clusters have stopped growing, this growth and merge stage of the algorithm terminates.

We keep track of the growing clusters in the Cluster Growth Stack (CGS) data structure. It contains an entry for each defect, and each entry contains three pieces of information:

1. A *vertex_id* to represent which defect the entry is for.
2. A *growth_radius* to represent how far this defect has grown. The maximum required distance a defect will have to grow depends on the structure of a decoding graph.
3. A *valid_bit*, set to 1 if this defect should be grown in the next round of growth, and set to 0 otherwise.

In the CGS the growth step is performed by updating the growth radius for the valid entries of the stack. This is a single read and write operation per defect.

To keep track of which cluster a vertex belongs to, we use the Parent Table. It has an address in memory for each defect holding the address of the corresponding parent defect. Upon initialisation, each defect is its own parent. We call any such entry with this property a root. When two clusters merge, we set the root of one cluster equal to the root of the other cluster. The choice of which cluster to update is arbitrary.

To determine if two clusters merge, we take each pair of defects (one defect from each cluster), calculate the distance between them in the decoding graph, and check if the sum of their growths is greater than this distance. If it is, the two clusters merge. For a CGS with s entries, this leads to $s^2/2$ of these *collision* detection comparisons.

The key to checking cluster mergers is efficient computation of the distance between two defects along the edges of the graph. In a general graph, this can be implemented using a lookup table of pre-computed distances. Here, we further minimise the power and area requirements of the design by exploiting the structure of the surface code to develop combinatorial functions that compute the distances without the need to traverse the graph. The structure of the decoding graphs is essentially encoded in these functions, and it leads to fast collision detection operations. For a phenomenological noise model, this function

will consist of computing the Manhattan distance on a cubic lattice, with modifications to account for boundaries. Further modifications are required to account for extra space-time edges when using the circuit-level noise model.

IV. COLLISION CLUSTERING MICRO-ARCHITECTURE

In this section we describe the micro-architecture of the CC decoder, shown in Fig. 2b. It is composed of shared memories and registers, and three processing units: Initialisation, Growth and Merge.

A. Shared memories and registers

The processing units are supplemented by a set of internal memories and registers keeping the intermediary computational state. The growth of the clusters is tracked in the Cluster Growth Stack memory as described in Section III. Recall also that the Parent Table keeps track of the clusters; each defect is represented by an address in memory, and the data represents its corresponding parent defect. Additionally, three registers keep track of parameters for each growing cluster, the Boundary, Logical and Parity registers. In each register, a defect is represented by an address. For the Boundary and Logical registers, the bit is set if the corresponding cluster touches the boundary, respectively logical boundary. In the parity register, the bit is set if the parity of the cluster is odd.

B. Processing units

The *Init* unit is active on first initialisation of the decoder with a new syndrome and configuration. It is responsible for processing the decoder configuration, loading of the input syndrome data and loading the appropriate data into the storage elements.

The *Grow* unit is responsible for the growth stage of the algorithm, as outlined in Section III. It updates the Cluster Growth Stack cluster entries at every iteration, finding the root of a cluster, then writing the radius and validity status. While processing a cluster, the *Grow* unit also checks for collisions with either boundary, writing the colliding vertex and the virtual boundary or virtual logical vertex to the Merge stack. Finally, the *Grow* unit also simultaneously computes the logical correction bit resulting from the growth stage. The correction is discarded and recomputed on the next growth cycle if growth is required, or is kept and used as the correction output on successful termination of the decode cycle.

The *Merge* unit is composed of *Match* and *Union* sub-units, which operate in parallel. At every iteration, the *Match* sub-unit performs collision detection comparisons

from CGS data. It then writes colliding defect pairs onto the Merge stack. The *Union* sub-unit reads collided vertex entries from the Merge stack, then searches the Parent Table for the two roots. It then updates the Parent Table, Logical, Boundary and Parity registers with the results of the clusters' union.

The execution of the algorithm and the associated data structures are shown on a simple example in Fig. 2a and the associated micro-architecture in Fig. 2b.

V. PHYSICAL IMPLEMENTATION

A. FPGA

In Table I we present the performance of our FPGA implementation of decoding the rotated planar surface code across a range of distances from 3 to 23 using the CC decoder. The specific FPGA used is the Xilinx Ultrascale+ XCVU3P [36]. We see that the FPGA decoder can decode below the $1\mu\text{s}$ threshold up to distance 21. The maximum clock frequency (FMax) targeted for this implementation is 400 MHz. It can be seen that due to the low resource utilisation, FMax is not significantly impacted by increasing the distance of the code.

The precise resource requirements of the FPGA, including the percentage of resource utilised, are also given in Table I. The only resources required to implement CC are trivial logic gates along with storage elements. Notably, no Digital Signal Processing (DSP) elements are used, whose use would increase the area of the implementation. While results are only provided up to distance 23, based on the utilisation percentages, fitting larger distance instances of the decoder onto the FPGA will be straightforward.

As explained in Section III, one of the main advantages of the CC decoder is the efficient use of storage resources. Fig. 3d shows, for each code distance, the storage required for each of the main data structures. The micro-architecture has other storage elements e.g. Boundary, Logical and Parity registers. These are typically implemented as flip-flops and the overall results are given in Table I. For a distance 23 implementation, the main data structure storage requirement is around 13 KB which is a third of a level-1 data cache size in a typical application CPU. Similar to these caches on CPUs, the CC memories can be accessed at very high frequencies in a single clock cycle, enabling performant data processing.

Some of the other known FPGA based hardware decoders [14, 15] require substantial resources at larger code distances. The data structures are also sized based on a phenomenological noise model at $p = 10^{-3}$, so they have significantly under-counted resources compared to the requirements for a circuit-level noise model of the same magnitude.

As well as being performant and resource efficient, our implementation needs to be accurate, that is, effectively suppress physical errors. We demonstrate that

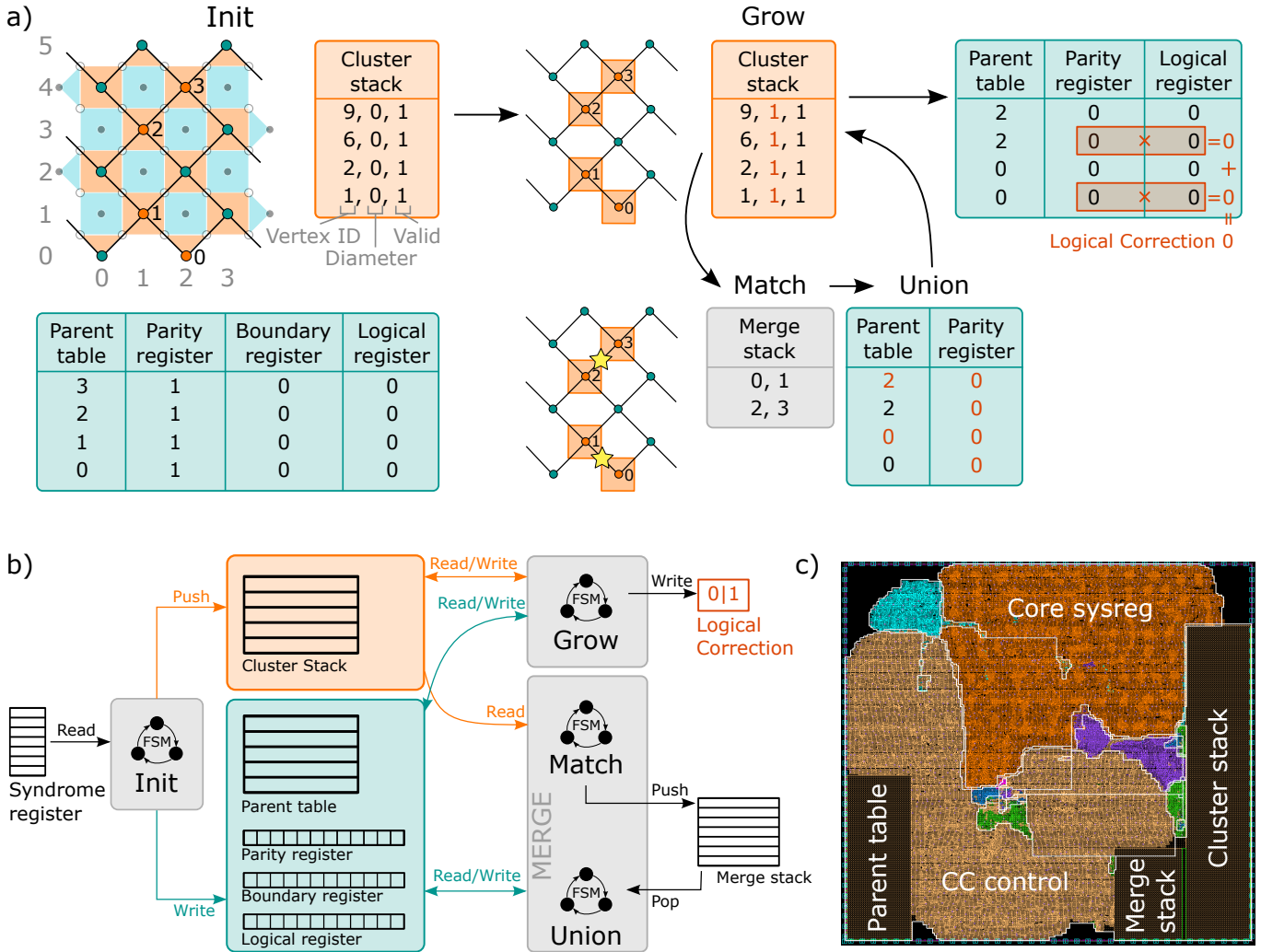


FIG. 2. Collision clustering decoder. (a) Schematic of the CC decoder on an example of a single round of a rotated planar surface code. First, in the Init step, the data structures are initialised with every defect being its own parent. In the main loop, the Grow step calculates the validity of the clusters and increases the diameter of all valid clusters. The clusters are checked for collisions in the Merge step and colliding pairs of clusters are pushed to the Merge stack. The Union step pops the pairs from the Merge stack, makes one cluster root the root of the other, and updates the parity, boundary and logical registers of the root of the cluster. When all clusters are invalidated, the final logical correction is calculated. (b) Micro-architecture diagram of the CC decoder computation engine, with annotated data flow. The input and output of the decoder is accessible through programmable registers. The logical correction bit is recalculated on the fly during Grow. The Merge processing element consists of Match and Union sub-units active in parallel. (c) The floorplan of a distance $d = 23$ ASIC implementing the CC decoder. Annotated: *Parent Table*, *Merge Stack* and *Cluster Stack* SRAM cells; *CC control* logic formed of Init, Grow, and Merge processing units that are implemented as Finite State Machines (FSM). *Core sysreg* logic contains input syndrome registers, control registers and the Metric Generation Unit. Other coloured regions contain clocking, IO and other miscellaneous logic.

our FPGA CC implementation is indeed accurate using a threshold plot [25] given in Fig. 3a. Our implementation has a threshold of 0.78%, which means that for values of p less than this errors are suppressed exponentially by increasing the code distance.

B. ASIC

In Table II we present two physical implementations of the CC decoder on a 12 nm FinFET process node: decoding a distance 7 and a distance 23 surface code. They respectively take 10 ns and 240 ns to decode one round of syndrome measurements, using only 2.75 mW and 7.85 mW of power. In the near term, we believe that the distance 7 instance will be valuable in testing

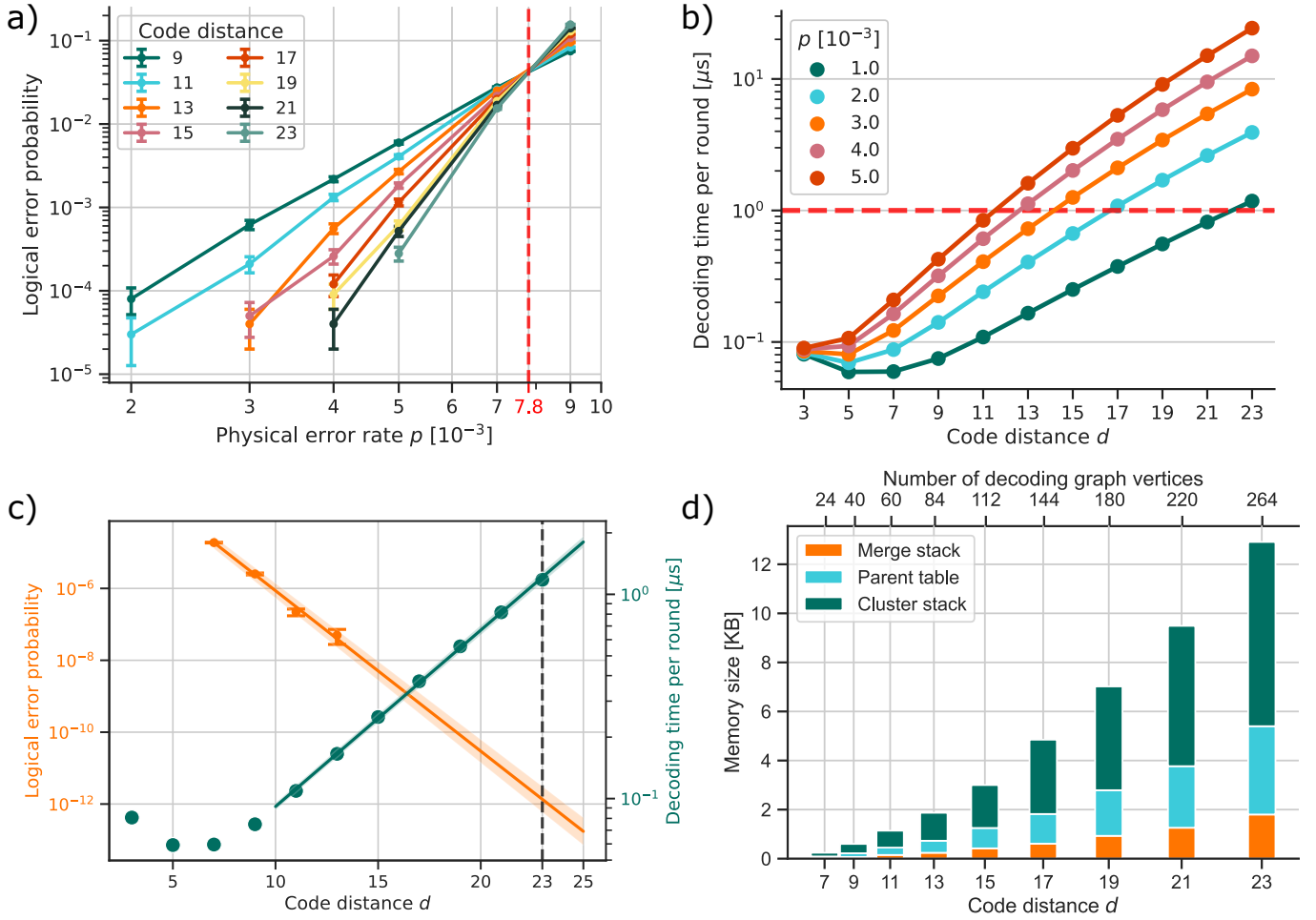


FIG. 3. Performance of our FPGA implementation of the CC decoder on the rotated planar surface code. (a) Logical error probability for varying physical error rate p and a range of code distances demonstrating threshold at around $p = 7.8 \times 10^{-3}$. Each point is acquired with 10^5 samples. (b) Decoding time per syndrome measurement round as a function of code distance for different noise rates. Even at a high noise just below threshold ($p = 0.5\%$) expected in near-term hardware, our decoder can decode large ($d = 11$) codes at sub- $1\mu\text{s}$ per round rate. (c) Decoding time per round at $p = 0.1\%$ together with a projection of logical error probability to large distance regime. The decoder is just short of $1\mu\text{s}$ per round at distance $d = 23$ on the affordable Xilinx Ultrascale+ XCVU3P hardware while expected logical error probability is of the order of 10^{-12} . Each accuracy point was obtained using 10^8 samples. (d) FPGA memory size usage of different data structures for varying code distances using $p = 0.1\%$. Even at distance $d = 23$ the decoder uses below 13 KB of memory, allowing for implementation on affordable FPGA hardware.

error correction experiments with cryogenic CMOS based control systems.

A floorplan defines the approximate locations, sizes and shapes of various logical blocks of the design. The floorplan helps to determine how signals will interact between different blocks, which enables optimization for performance, power and area. The floorplan for a distance 23 implementation is shown in Fig. 2c. We have integrated SRAM macros as storage elements for the Cluster Stack, Merge Stack and the Parent Table. For all other storage elements, flip-flops are used from the MultiVt standard cell libraries. This enables a good balance between optimizing for performance, power and area.

VI. DISCUSSION

A. Related work

To the best of our knowledge, there have been four demonstrations of decoders implemented on dedicated classical hardware [14–17]. Lookup table decoders are implemented on FPGAs in [14] and [17]. In both cases, the error correction scheme demonstrated is relatively simple; the distance 3 repetition code [17], and the distance 5 surface code [14]. The exponentially scaling memory requirements make lookup table decoders impractical for surface code distances above 5.

In [16], the authors implement a neural network decoder on an FPGA. Measurement errors are not con-

Code Distance	FPGA Performance		FPGA Utilisation				
	Fmax [MHz]	Exec-time [μ s]	Logic LUTs	LUTRAMs	FlipFlops	RAMB36	RAMB18
3	449	0.07	2491 (0.63%)	12 (0.01%)	1572 (0.20%)	0 (0.00%)	0 (0.00%)
5	445	0.06	2709 (0.69%)	27 (0.01%)	1670 (0.21%)	0 (0.00%)	0 (0.00%)
7	406	0.06	3092 (0.78%)	49 (0.02%)	1984 (0.25%)	0 (0.00%)	0 (0.00%)
9	408	0.07	3800 (0.96%)	100 (0.05%)	2483 (0.32%)	0 (0.00%)	0 (0.00%)
11	412	0.11	4600 (1.17%)	68 (0.03%)	3591 (0.40%)	0 (0.00%)	1 (0.07%)
13	411	0.16	5914 (1.50%)	105 (0.05%)	4136 (0.52%)	0 (0.00%)	1 (0.07%)
15	403	0.25	7793 (1.96%)	60 (0.03%)	5432 (0.69%)	1 (0.14%)	1 (0.07%)
17	408	0.37	10446 (2.66%)	90 (0.05%)	7184 (0.91%)	1 (0.14%)	1 (0.07%)
19	402	0.55	13331 (3.38%)	0 (0.00%)	9277 (1.18%)	2 (0.28%)	2 (0.14%)
21	405	0.81	17237 (4.37%)	0 (0.00%)	11957 (1.52%)	2 (0.28%)	2 (0.14%)
23	401	1.18	21693 (5.50%)	0 (0.00%)	15126 (1.92%)	5 (0.69%)	1 (0.07%)

TABLE I. FPGA results for decoding the rotated planar surface code. (a) Code distance: the size of the error correcting code. (b) Fmax: the maximum achieved clock frequency on the targeted FPGA. (c) Exec-time: the execution time averaged over 100,000 shots, normalised by dividing by the d rounds of syndrome generation. (d) Logic LUTs: the number of FPGA lookup tables used for logic primitives. (e) LUTRAMs, FF, RAMB36 and RAMB18: different types of storage elements. The mapping of CC data structures to a storage element depend on the size of the structure. The numbers in round bracket are the percentage of the corresponding type of resource used on the FPGA.

Code Distance	ASIC Performance		ASIC Area		ASIC Power	
	Fmax [MHz]	Exec-time [μ s]	Die-size [mm^2]	FlipFlops	Dynamic [mW]	Leakage [mW]
7	2000	0.01	0.009	3957	2.73	0.02
23	2000	0.24	0.064	15840	7.72	0.13

TABLE II. CC ASIC results for decoding the rotated planar surface code using a 12 nm FinFET process assuming $p=0.1\%$. We use industry-leading EDA tools to determine the frequency of the implementation. To calculate the execution time, we use this frequency along with the cycle counts of the FPGA implementations.

sidered, limiting its effectiveness and understanding of how the decoder will perform with experimental qubits. Moreover, on an FPGA, they are restricted to a distance 5 surface code. Additionally, the corresponding estimated performance, power and area of the ASIC synthesis all degrade significantly when increasing the distance from 3 to 5, implying that the design will not effectively scale.

The most significant prior implementation of a surface code decoder on classical hardware is found in [15]. The authors demonstrate a highly distributed implementation Union-Find on an FPGA, assuming a phenomenological noise model. Each vertex of the decoding graph is assigned a processing unit, and communication across the design is limited e.g. typically only nearest neighbour processing units can communicate with each other. They report that a round of syndrome measurements for a distance 21 surface code can be decoded in 11.5 ns on an FPGA. Given that circuit-level noise results in more defects (Fig. 1d), this performance would be slower if the authors extended their noise model to circuit-level noise. Furthermore, a consequence of this highly distributed approach is that large numbers of lookup tables (LUTs) and registers are required for the implementation (900k LUTs and 240k registers). Registers are necessary in a

distributed implementation so that data can be accessed at the same time in a few number of cycles. However, a register can be an order of magnitude bigger in size and power consumption compared to a bit in memory. This is reasonable when only a few hundred registers are needed, but if thousands or more are required, this difference becomes significant. Hence, the numbers reported by the authors will lead to a large area and power consumption, and will increase the cost of any chip developed. This would prevent any such design from being integrated as part of decode compute close to the cryo-substrate, for instance as part of a cryogenic control system.

As mentioned above, Das et al. [18] propose a micro-architecture for the Union-Find decoding algorithm, and model decoding a distance 11 surface code. In addition to only considering phenomenological noise, the authors observe that their micro-architecture is dominated by memory. As memory sizes increase with increasing surface code distance, latency will also increase due to the time needed to read and write from and to the memory. No implementation or cycle-accurate simulation of this decoder is provided limiting the understanding of how the increased memory size affects performance. The authors also assume a 4 GHz frequency, which can be challenging to obtain.

Finally, there are also implementations of decoders in SFQ (Single Flux Quantum) logic [37, 38]. In these implementations, only relatively small surface code distances are considered and simple noise models are used. Moreover, the lack of maturity of the technology compared to CMOS, in both capabilities (see [18]) and the supporting ecosystem, means that implementing decoders in SFQ logic which can operate at scale will be challenging.

B. Application to other codes

In the future, different target applications will require different code distances based on the length of the computation to be performed. For this reason, decoding hardware that can only deal with a very specific code and code distance has limited value in the real-world.

The Union-Find algorithm itself is very flexible. It works for the same family of codes as minimum weight perfect matching, i.e. any code for which a meaningful decoding graph can be derived. In the hardware proposal of Das et al. [18], some flexibility of the Union-Find algorithm is lost, as the exact structure of the decoding graph is implicitly represented by the layout of the STM, and changing this would require all the accesses and address translation for use of the STM to also change. In CC the decoding graph is encoded by the distance calculation function, and this is the only part of the design that has to change based on the code. While CC is more flexible than other proposed hardware implementations of Union-Find, the current implementation is optimised for the surface codes where efficient closed form distance functions exist. For more general decoding graphs that do not have efficient closed-form distance functions, the design would have to be adapted to include a lookup table of distances.

VII. CONCLUSION

In this work we introduced the Collision Clustering (CC) decoding algorithm and described a micro-architecture for its implementation. Fault-tolerant quantum computing requires a decoder to process error syndromes at speed in order to prevent a decoding backlog that exponentially slows down the logical clock rate. Moreover, any scalable quantum computer requires a decoder to be resource efficient, which will also enable tight integration with control systems in a cryogenic environment. Demonstrations of cryogenic CMOS based control systems are showing promising results [39–41] and tightly integrating a decoder will provide the most cost-effective system. Current cryogenic systems however have a strict power budget, in the order of 1 W at the 4 K temperature range [42]. We envisage that this will result in a power budget of 10s of mW for a decoder, so that the predominant power budget is reserved for qubit control and

readout. To help meet these requirements, we designed CC to be memory and power efficient. While CC has a quadratic asymptotic scaling, we show this is remedied with parallelisation and pipelining for the relevant code distances, demonstrating that CC is a scalable, fast and highly resource efficient decoder.

To verify that the CC decoder satisfies the performance, power and area requirements, we implemented it on both an FPGA and ASIC. We decode a logical memory experiment using large distance surface code examples in under 1 μ s per syndrome measurement round assuming a $p = 0.1\%$ circuit-level noise model. On the FPGA we showed that CC can decode a distance 21 surface code in 810 ns per syndrome measurement round, utilising only 4.5% of a modest sized FPGA (a Xilinx Ultrascale+ XCVU3P). Using a modern 12 nm FinFET process node, we showed that CC can decode a distance 23 surface code in 210 ns per syndrome measurement round using only 0.06 mm² area and 8 mW power.

The logical memory experiment simulated in this work preserves a state for a finite time period. To preserve a logical state indefinitely, *sliding window decoding* [34] can be used. While continuous rounds of syndrome measurements are being generated, the decoder processes only a contiguous set, or *window*, of these rounds. Utilising the whole window, the decoder commits to a correction for the longer lived defects in the window, storing it in software. The window then slides up to include more recent rounds of measurements, the process repeats, and the correction updated. Certain boundary effects make this process more complex than the one simulated in this work. Therefore, developing a fast and efficient sliding window implementation of CC will be an important next step in the advancement of decoders for fault-tolerant computation.

VIII. ACKNOWLEDGEMENTS

We thank Steve Brierley and Jake Taylor for encouraging this research and related discussions. We also thank Maria Maragkou for feedback on the manuscript.

- [1] C. J. Ballance, T. P. Harty, N. M. Linke, M. A. Sepiol, and D. M. Lucas, *Physical Review Letters* **117**, 060504 (2016).
- [2] R. Acharya, I. Aleiner, R. Allen, T. I. Andersen, M. Ansmann, F. Arute, K. Arya, A. Asfaw, J. Atalaya, R. Babush, D. Bacon, J. C. Bardin, J. Basso, A. Bengtsson, S. Boixo, G. Bortoli, A. Bourassa, J. Bovaird, L. Brill, M. Broughton, B. B. Buckley, D. A. Buell, T. Burger, B. Burkett, N. Bushnell, Y. Chen, Z. Chen, B. Chiaro, J. Cogan, R. Collins, P. Conner, W. Courtney, A. L. Crook, B. Curtin, D. M. Debroy, A. Del Toro Barba, S. Demura, A. Dunsworth, D. Eppens, C. Erickson, L. Faoro, E. Farhi, R. Fatemi, L. Flores Burgos, E. Forati, A. G. Fowler, B. Foxen, W. Giang, C. Gidney, D. Gilboa, M. Giustina, A. Grajales Dau, J. A. Gross, S. Habegger, M. C. Hamilton, M. P. Harrigan, S. D. Harrington, O. Higgott, J. Hilton, M. Hoffmann, S. Hong, T. Huang, A. Huff, W. J. Huggins, L. B. Ioffe, S. V. Isakov, J. Iverson, E. Jeffrey, Z. Jiang, C. Jones, P. Juhas, D. Kafri, K. Kechedzhi, J. Kelly, T. Khattar, M. Khezri, M. Kieferová, S. Kim, A. Kitaev, P. V. Klimov, A. R. Klots, A. N. Korotkov, F. Kostritsa, J. M. Kreikebaum, D. Landhuis, P. Laptev, K.-M. Lau, L. Laws, J. Lee, K. Lee, B. J. Lester, A. Lill, W. Liu, A. Locharla, E. Lucero, F. D. Malone, J. Marshall, O. Martin, J. R. McClean, T. McCourt, M. McEwen, A. Megrant, B. Meurer Costa, X. Mi, K. C. Miao, M. Mohseni, S. Montazeri, A. Morvan, E. Mount, W. Mruczkiewicz, O. Naaman, M. Neeley, C. Neill, A. Nersisyan, H. Neven, M. Newman, J. H. Ng, A. Nguyen, M. Nguyen, M. Y. Niu, T. E. O'Brien, A. Opremcak, J. Platt, A. Petukhov, R. Potter, L. P. Pryadko, C. Quintana, P. Roushan, N. C. Rubin, N. Saei, D. Sank, K. Sankaragomathi, K. J. Satzinger, H. F. Schurkus, C. Schuster, M. J. Shearn, A. Shorter, V. Shvarts, J. Skrzynny, V. Smelyanskiy, W. C. Smith, G. Sterling, D. Strain, M. Szalay, A. Torres, G. Vidal, B. Villalonga, C. Vollgraft Heidweiller, T. White, C. Xing, Z. J. Yao, P. Yeh, J. Yoo, G. Young, A. Zalcman, Y. Zhang, N. Zhu, and G. Q. AI, *Nature* **614**, 676 (2023).
- [3] W. Huang, C. H. Yang, K. W. Chan, T. Tanttu, B. Hensen, R. C. C. Leon, M. A. Fogarty, J. C. C. Hwang, F. E. Hudson, K. M. Itoh, A. Morello, A. Laucht, and A. S. Dzurak, *Nature* **569**, 532 (2019), 1805.05027.
- [4] D. Litinski and N. Nickerson, Active volume: An architecture for efficient fault-tolerant quantum computers with limited non-local connections (2022), [arXiv:2211.15465 \[quant-ph\]](https://arxiv.org/abs/2211.15465).
- [5] B. M. Terhal, *Rev. Mod. Phys.* **87**, 307 (2015).
- [6] L. Skoric, D. E. Browne, K. M. Barnes, N. I. Gillespie, and E. T. Campbell, Parallel window decoding enables scalable fault tolerant quantum computation (2022), [arXiv:2209.08552 \[quant-ph\]](https://arxiv.org/abs/2209.08552).
- [7] O. Higgott and C. Gidney, Sparse blossom: correcting a million errors per core second with minimum-weight matching (2023), [arXiv:2303.15933 \[quant-ph\]](https://arxiv.org/abs/2303.15933).
- [8] O. Higgott, T. C. Bohdanowicz, A. Kubica, S. T. Flammia, and E. T. Campbell, *Phys. Rev. X* **13**, 031007 (2023).
- [9] Y. Wu and L. Zhong, Fusion blossom: Fast MWPM decoders for QEC (2023), [arXiv:2305.08307 \[quant-ph\]](https://arxiv.org/abs/2305.08307).
- [10] J. Ferreira Marques, B. Varbanov, M. Moreira, H. Ali, N. Muthusubramanian, C. Zachariadis, F. Battistel, M. Beekman, N. Haider, W. Vlothuizen, A. Bruno, B. Terhal, and L. DiCarlo, *Nature Physics* **18**, 80 (2021).
- [11] S. Krinner, N. Lacroix, A. Remm, A. Di Paolo, E. Genois, C. Leroux, C. Hellings, S. Lazar, F. Swiadek, J. Herrmann, G. J. Norris, C. K. Andersen, M. Müller, A. Blais, C. Eichler, and A. Wallraff, *Nature* **605**, 669 (2022).
- [12] L. Postler, S. Heußen, I. Pogorelov, M. Rispler, T. Feldker, M. Meth, C. D. Marciniak, R. Stricker, M. Ringbauer, R. Blatt, P. Schindler, M. Müller, and T. Monz, *Nature* **605**, 675 (2022).
- [13] D. Litinski, *Quantum* **3**, 128 (2019).
- [14] P. Das, A. Locharla, and C. Jones, in *Proceedings of the 27th ACM International Conference on Architectural Support for Programming Languages and Operating Systems*, ASPLOS '22 (Association for Computing Machinery, 2022) p. 541–553.
- [15] N. Liyanage, Y. Wu, A. Deters, and L. Zhong, Scalable quantum error correction for surface codes using FPGA (2023), [arXiv:2301.08419 \[quant-ph\]](https://arxiv.org/abs/2301.08419).
- [16] R. J. Overwater, M. Babaie, and F. Sebastiano, *IEEE Transactions on Quantum Engineering* **3**, 1 (2022).
- [17] D. Ristè, L. C. G. Govia, B. Donovan, S. D. Fallek, W. D. Kalfus, M. Brink, N. T. Bronn, and T. A. Ohki, *npj Quantum Information* **6**, 71 (2020).
- [18] P. Das, C. A. Pattison, S. Manne, D. M. Carmean, K. M. Svore, M. Qureshi, and N. Delfosse, in *2022 IEEE International Symposium on High-Performance Computer Architecture (HPCA)* (2022) pp. 259–273.
- [19] E. Charbon, F. Sebastiano, A. Vladimirescu, H. Homulle, S. Visser, L. Song, and R. M. Incandela, in *2016 IEEE International Electron Devices Meeting (IEDM)* (2016) pp. 13.5.1–13.5.4.
- [20] ASIC implementation means the design has been signed-off using industry-leading Electronic Design Automation (EDA) tooling, top-tier foundry silicon-proven multi-Vt libraries, SRAM IP and spice models. This ensures high quality results which include all the fabrication process variations of device models and parasitic effects from the power network, clock-tree synthesis, place and route stages.
- [21] A. Y. Kitaev, *Annals of physics* **303**, 2 (2003).
- [22] C. Chamberland and E. T. Campbell, *PRX Quantum* **3**, 010331 (2022).
- [23] A. G. Fowler and C. Gidney, Low overhead quantum computation using lattice surgery (2018), [arXiv:1808.06709 \[quant-ph\]](https://arxiv.org/abs/1808.06709).
- [24] D. Horsman, A. G. Fowler, S. Devitt, and R. V. Meter, *New Journal of Physics* **14**, 123011 (2012).
- [25] A. G. Fowler, A. M. Stephens, and P. Groszkowski, *Phys. Rev. A* **80**, 052312 (2009).
- [26] Y. Tomita and K. M. Svore, *Phys. Rev. A* **90**, 062320 (2014).
- [27] C. Gidney and M. Ekerå, *Quantum* **5**, 433 (2021).
- [28] J. Lee, D. W. Berry, C. Gidney, W. J. Huggins, J. R. McClean, N. Wiebe, and R. Babbush, *PRX Quantum* **2**, 030305 (2021).
- [29] T. Häner, S. Jaques, M. Naehrig, M. Roetteler, and M. Soeken, in *Post-Quantum Cryptography*, edited by J. Ding and J.-P. Tillich (Springer International Pub-

- lishing, Cham, 2020) pp. 425–444.
- [30] C. Gidney, M. Newman, A. Fowler, and M. Broughton, *Quantum* **5**, 605 (2021).
- [31] N. S. Blunt, J. Camps, O. Crawford, R. Izsák, S. Leontica, A. Mirani, A. E. Moylett, S. A. Scivier, C. Sünderhauf, P. Schopf, J. M. Taylor, and N. Holzmann, *Journal of Chemical Theory and Computation* **18**, 7001 (2022), PMID: 36355616.
- [32] M. E. Beverland, P. Murali, M. Troyer, K. M. Svore, T. Hoefler, V. Kliuchnikov, G. H. Low, M. Soeken, A. Sundaram, and A. Vaschillo, Assessing requirements to scale to practical quantum advantage (2022), [arXiv:2211.07629 \[quant-ph\]](https://arxiv.org/abs/2211.07629).
- [33] C. Gidney, *Quantum* **5**, 497 (2021).
- [34] E. Dennis, A. Kitaev, A. Landahl, and J. Preskill, *Journal of Mathematical Physics* **43**, 4452 (2002).
- [35] N. Delfosse and N. H. Nickerson, *Quantum* **5**, 595 (2021).
- [36] Xilinx ultrascale+ datasheet (2021), <https://docs.xilinx.com/v/u/en-US/ds923-virtex-ultrascale-plus>. Accessed: 06/09/2023.
- [37] A. Holmes, M. R. Jokar, G. Pasandi, Y. Ding, M. Pedram, and F. T. Chong, in *Proceedings of the ACM/IEEE 47th Annual International Symposium on Computer Architecture*, ISCA '20 (IEEE Press, 2020) pp. 556–569.
- [38] Y. Ueno, M. Kondo, M. Tanaka, Y. Suzuki, and Y. Tabuchi, in *2021 58th ACM/IEEE Design Automation Conference (DAC)* (IEEE, 2021) pp. 451–456.
- [39] D. J. Frank, S. Chakraborty, K. Tien, P. Rosno, T. Fox, M. Yeck, J. A. Glick, R. Robertazzi, R. Richetta, J. F. Bulzacchelli, D. Ramirez, D. Yilma, A. Davies, R. V. Joshi, S. D. Chambers, S. Lekuch, K. Inoue, D. Underwood, D. Wisnieff, C. Baks, D. Bethune, J. Timmerwilke, B. R. Johnson, B. P. Gaucher, and D. J. Friedman, in *2022 IEEE International Solid-State Circuits Conference (ISSCC)*, Vol. 65 (2022) pp. 360–362.
- [40] J. C. Bardin, E. Jeffrey, E. Lucero, T. Huang, S. Das, D. T. Sank, O. Naaman, A. E. Megrant, R. Barends, T. White, M. Giustina, K. J. Satzinger, K. Arya, P. Roushan, B. Chiaro, J. Kelly, Z. Chen, B. Burkett, Y. Chen, A. Dunsworth, A. Fowler, B. Foxen, C. Gidney, R. Graff, P. Klimov, J. Mutus, M. J. McEwen, M. Nealey, C. J. Neill, C. Quintana, A. Vainsencher, H. Neven, and J. Martinis, *IEEE Journal of Solid-State Circuits* **54**, 3043 (2019).
- [41] S. J. Pauka, K. Das, R. Kalra, A. Moini, Y. Yang, M. Trainer, A. Bousquet, C. Cantaloube, N. Dick, G. C. Gardner, M. J. Manfra, and D. J. Reilly, *Nature Electronics* **4**, 64 (2021).
- [42] S. Krinner, S. Storz, P. Kurpiers, P. Magnard, J. Heinsoo, R. Keller, J. Lütolf, C. Eichler, and A. Wallraff, *EPJ Quantum Technology* **6**, 1 (2019).